Micromechanical constitutive modelling of granular media: evolution and loss of contact in particle clusters

B.S. GARDINER and A. TORDESILLAS*

Department of Mathematics and Statistics, The University of Melbourne, Victoria 3010, Australia
(atordesi@ms.unimelb.edu.au)

Abstract. Micromechanical constitutive equations are developed which allow for the broad range of interparticle interactions observed in a real deforming granular assembly: microslip contact, gross slip contact, loss of contact and an evolution in these modes of contact as the deformation proceeds. This was accomplished through a synergetic use of contact laws, which account for interparticle resistance to both sliding and rolling, together with *strain-dependent* anisotropies in contacts and the normal contact force. By applying the constitutive model to the bi-axial test it is demonstrated that the model can correctly predict the evolution of various anisotropies as well as the formation of a distinct shear band. Moreover, the predicted shear-band properties (*e.g.* thickness, prolonged localisation, void ratio) are an even better fit with experimental observations than were previously found by use of previously developed micromechanical models.

Key words: anisotropy, fabric evolution, granular media

1. Introduction

Tordesillas and Walsh [1] developed a framework for constructing micropolar constitutive models for dry monodisperse granular materials. Their method is based on averaging the interactions within a particle cluster, which consists of a single particle and its immediate neighbours (see Figure 1). By considering only a small number of particles in its representative volume element, their method diverges from many previous micromechanical models, with the subsequent advantage that this high-resolution technique should be capable of capturing microstructures consisting of only a few particles *e.g.* shear bands. The generalised constitutive relations derived in their paper were as follows:

$$\sigma_{\alpha\beta} = \frac{1-\upsilon}{\pi R} \int_{\Omega} f_{\alpha} n_{\beta} \Phi \mathrm{d}\boldsymbol{n}, \tag{1.1}$$

$$\mu_{\alpha} = \frac{1-\upsilon}{\pi R} \int_{\Omega} \left[M n_{\alpha} + R e_{\beta\phi 3} f_{\beta} n_{\alpha} n_{\phi} \right] \Phi \mathrm{d}\boldsymbol{n}, \tag{1.2}$$

where $\sigma_{\alpha\beta}$ is the $\alpha\beta$-component of stress, μ_{α} is the α-component of couple stress, R is the particle radius, υ is the void ratio of the Voronoi cell (ratio of the void volume to the total volume of the cell), f_{α} is the α-component of the contact force, n_{β} is the β-component of the outward unit vector $\boldsymbol{n}$ from the particle centre in the direction of contact, M is the rolling resistance, $e_{\beta\phi 3}$ is the permutation symbol, and Ω represents all possible orientations in space. A repeated subscript signifies a summation over the range of the repeated subscript (in a two-dimensional model the summation is from 1 to 2). The weighting function Φ represents
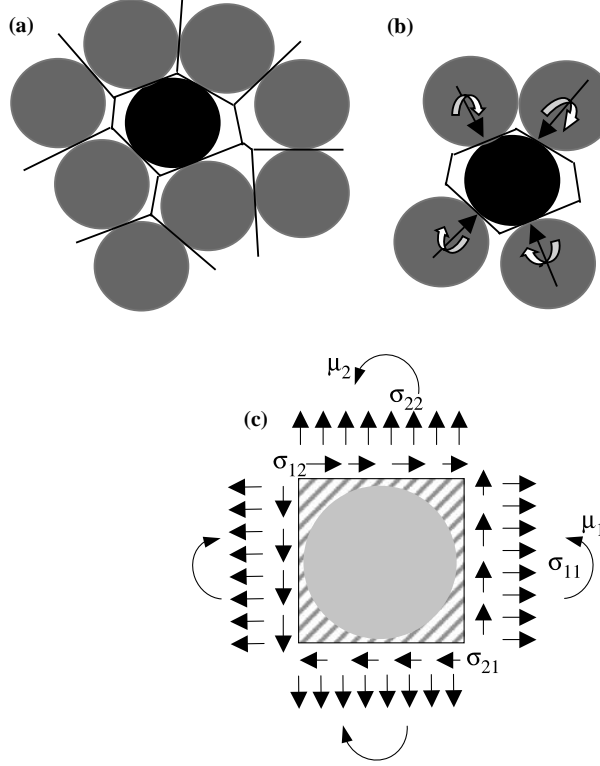
Figure 1. The homogenisation process employed by Tordesillas and Walsh [1]: (a) a Voronoi tessellation of the discrete assembly yields a Voronoi cell for each particle and its immediate void space, (b) interactions between a particle and its contacting neighbours (*i.e.*, forces and moments at contacts) are averaged over the particle's Voronoi cell, (c) corresponding micropolar continuum element of the same area as that of the Voronoi cell.

the angular-contact-density distribution function, and describes the probability of finding a contacting particle for a given direction. Hence, for a particle with N neighbouring contacts, it follows that

$$\int_{\Omega} \Phi \, d\boldsymbol{n} = N.$$

The function Φ may be used to introduce contact anisotropy. The form of this angular-contact-density distribution function, however, remains an open problem and is an area in need of further investigation. It has been established experimentally that particle arrangements (fabric) and rearrangements (fabric evolution) govern bulk behaviour of granular media. A summary of key experimental findings on fabric evolution is given in [2, Chapter 4]. In particular, it has been observed that contacts within a granular material tend to align themselves in the direction of maximum compressive strain [3]. To account for this experimental result, Walsh and Tordesillas [4] adopted a bipolar contact-density distribution function in which the highest probability of finding a contact was aligned with the direction of maximum compressive strain. The form of their contact-density distribution function is shown in Figure 2 and defined by

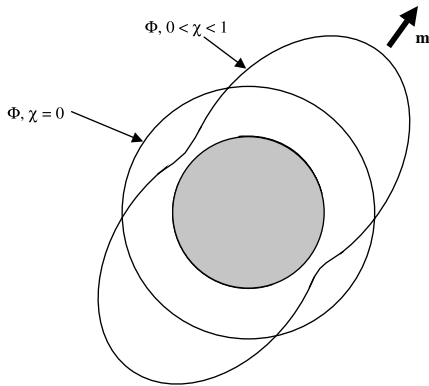$$\Phi(\boldsymbol{n}, \boldsymbol{m}, \chi, \nu) = \frac{N}{2\pi} \left(1 + \chi \cos(2\theta) \right), \tag{1.3}$$

Figure 2. The contact density distribution function Φ, in polar coordinates, for the isotropic case $\chi = 0$, and the anisotropic case $0 < \chi \leq 1$.
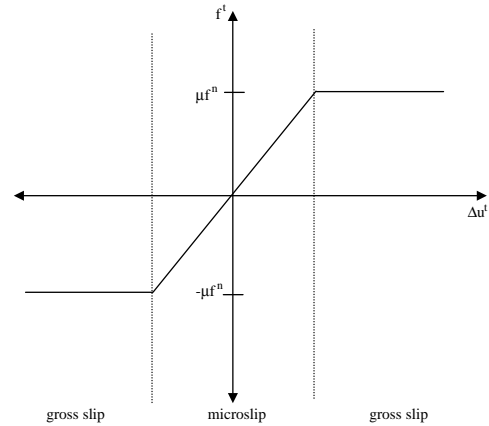

Figure 3. Graphical representation of Coulomb's law (Equation (2.5)).

where χ, the degree of the initial contact anisotropy, can take values in the range $0 < \chi \leq 1$. The symbol θ is defined by $\cos\theta = \boldsymbol{m} \cdot \boldsymbol{n}$, where the 'dot' denotes the scalar product and $\boldsymbol{m}$ is the unit vector pointing in the direction of greatest probability of finding a contacting neighbour. The drawback of this approach is that it limits the fabric evolution to a predefined mode of deformation, which may compromise a model's ability to predict the development of certain anisotropies arising in the formation and evolution of highly localised structures like shear bands (*e.g.* see [2, Chapter 4], [5]). In contrast, Tordesillas and Walsh [1] use an angular contact-density distribution function in which the maximum probability of finding a contact is aligned with the direction of highest density increase. This direction is given by the negative of the gradient of the void-ratio distribution function. In such a case, the contact anisotropy is able to evolve as the assembly deforms, since the void ratio is linked with strain; however, in practice the model was difficult to use without resorting to further simplifying assumptions regarding the evolution of the strain distribution throughout the whole assembly. Apart from these differences in the form for Φ, the two constitutive models [1,4], are identical. In particular, they both neglect: (i) gross slip and loss of contact, (ii) force anisotropy, and (iii) strain-dependent evolution in the force and contact anisotropy. In contrast with these previous models, this paper presents constitutive equations that allow for the possibility of microslip, gross slip and loss of contact. Contact laws, which describe these different modes of contact, are used in conjunction with strain-dependent contact forces, thereby allowing the current model to capture the evolution of these contact forces, the various modes of contact and contact anisotropy.

2. Incorporating gross slip, microslip and loss of contact

Forces and moments between contacting particles were not explicitly expressed in the previous discussion. Expressions for these contact forces and moments need to be inserted into the generalised constitutive laws, Equations (1.1) and (1.2), before the constitutive laws can be used. In this section, expressions are developed for contact forces and moments, which account for the broad range of interactions arising in real deforming granular media.

The contact force, appearing in (1.1) and (1.2), can be separated into normal f^n and tangential f^t components,

$$f_\alpha = f^n n_\alpha + f^t t_\alpha, \qquad (2.1)$$

where t_α is the α-component of the unit vector tangential to the contact. The normal force at a contact can be thought of as having two parts: (i) the initial normal force at a contact, and (ii) the normal force resulting from the relative normal displacement of contacting particles. If it is assumed that the particle deformation is linear elastic and that contacts are cohesionless, then the normal force at a contact can be written as

$$f^n = \begin{cases} f^{\text{initial}} + k^n \Delta u^n & \text{if } f^{\text{initial}} + k^n \Delta u^n < 0, \\ 0 & \text{if } f^{\text{initial}} + k^n \Delta u^n \geq 0, \end{cases} \qquad (2.2)$$

where f^{initial} is the initial normal contact force, k^n is the particle's normal stiffness coefficient, and Δu^n is the relative normal displacement of two contacting particles. The previous models of Tordesillas and Walsh [1] and Walsh and Tordesillas [4] assumed a constant f^n and so did not allow an evolution or loss of contacts.

It is well-accepted that the normal contact force (and for that matter, the tangential contact force) is not generally equal at all contacts, even prior to deformation. That is, particles rarely share forces equally amongst all neighbours. A striking demonstration of this normal contact force anisotropy can be seen in the photo-elastic disk experiments of Howell *et al.* [6]. In these experiments, it is clearly seen that particles tend to transmit forces through only 2 or 3 of their contacts, resulting in the so-called force chains. The other contacting particles can be considered to be spectator particles, as they have little or no contribution to the force transmission. Preferential force transmission occurs even prior to deformation of a granular material (*e.g.* static granular pile). To account for this potential normal force anisotropy, a weighting function, similar to that used for contact anisotropy (Equation (1.3)), can be combined with f^{initial}, such that the angular dependent normal force at a contact is expressed as

$$f^n(\theta) = \begin{cases} f^{\text{initial}}(1 + \chi^* \cos(2\theta + \phi)) + k^n \Delta u^n & \text{if } f^{\text{initial}}(1 + \chi^* \cos(2\theta + \phi)) + k^n \Delta u^n < 0, \\ 0 & \text{if } f^{\text{initial}}(1 + \chi^* \cos(2\theta + \phi)) + k^n \Delta u^n \geq 0. \end{cases} \qquad (2.3)$$

In (2.3), χ^* represents the degree of the initial normal contact-force anisotropy and can take values in the range $0 \leq \chi^* \leq 1$, with $\chi^* = 0$ corresponding to the isotropic case. Again, θ is defined by $\cos\theta = \boldsymbol{m} \cdot \boldsymbol{n}$ and ϕ is defined such that $\cos\frac{\phi}{2}$ represents the dot product between $\boldsymbol{m}$ and a unit vector in the direction of the maximum normal contact force. Note that the integrals, which, respectively, define the stress and couple stress in (1.1) and (1.2), are to be evaluated with respect to θ. By defining the normal contact force according to (2.3), not only has a potential initial normal contact-force anisotropy been introduced, but also the normal contact-force anisotropy is now able to evolve naturally with strain, as the relative normal displacement can be related to strain via:

$$\Delta u^n = 2R\varepsilon_{\alpha\beta} n_\alpha n_\beta, \qquad (2.4)$$

where $\varepsilon_{\alpha\beta}$ is the $\alpha\beta$-component of strain. Furthermore, an evolving anisotropy in the normal contact force results in an evolving angular-contact distribution, as contacts are lost in directions for which $f^{\text{initial}}(1 + \chi^* \cos(2\theta + \phi)) + k^n \Delta u^n \geq 0$.

In Equation (2.1), the tangential contact force can be related to the normal contact force by following Coulomb's contact law (see Figure 3) for the various modes of contact (*i.e.*, microslip and gross slip) and no contact:

$$
f^t = \begin{cases}
\text{sign}(\Delta u^t)\mu|f^n| & \text{if } |k^t\Delta u^t| \geq |\mu f^n| \text{ and } f^n < 0 \Rightarrow \text{gross slip}, \\
k^t\Delta u^t & \text{if } |k^t\Delta u^t| < |\mu f^n| \text{ and } f^n < 0 \Rightarrow \text{microslip}, \\
0 & \text{if } f^n \geq 0 \qquad\qquad\qquad \Rightarrow \text{no contact},
\end{cases}
\tag{2.5}
$$

where μ is the inter-particle friction coefficient, k^t is the particle's tangential stiffness coefficient, and Δu^t is the tangential component of the relative displacement of the contact points and is related to strain and curvature (gradient in rotation) κ_φ according to

$$
\Delta u^t = 2R\left(\varepsilon_{qr}n_r t_q - Rn_\varphi\kappa_\varphi\right),
\tag{2.6}
$$

such that

$$
\text{sign}\left(\Delta u^t\right) = \begin{cases}
1 & \text{if } \varepsilon_{qr}n_r t_q - Rn_\varphi\kappa_\varphi > 0, \\
-1 & \text{if } \varepsilon_{qr}n_r t_q - Rn_\varphi\kappa_\varphi < 0.
\end{cases}
\tag{2.7}
$$

Strictly speaking, the tangential contact force should have an additional term to represent the initial tangential contact force acting on a particle. However, the application of the current model is restricted to cases in which the granular specimen is prepared such that the expected initial tangential contact force is zero. Unlike the initial normal contact force, the initial tangential contact force may be either positive or negative, such that the expected initial tangential contact force in many circumstances will be close to zero. Applications for which the expected initial normal force may not be zero are, for now, not considered.

Since f^n has an evolving anisotropy, and f^t depends on f^n, it follows that f^t also has an evolving anisotropy. More specifically, not only do these contact laws (Equations (2.3) and (2.5)) allow the contact mode to be identified, but they also allow the direction of these contact modes to change with deformation, as the inequality constraints in Equation (2.5) contain an angular dependence due to the angular dependence of f^n and Δu^t. In other words, the mode of contact will vary with the direction of contact. At any stage in a granular media's deformation, a neighbouring particle pair will be sharing *only one* of the following: a microslip contact, a gross slip contact, or no contact. Therefore, the integration over the angle in Equations (1.1) and (1.2) can be separated into a sum of integrals, with each integral representing a contact mode (*i.e.*, gross slip or microslip) or no contact. That is, Equations (1.1) and (1.2) may be written as

$$
\sigma_{\alpha\beta} = \frac{1-\upsilon}{\pi R}\sum_{i=1}^{x}\left[\underbrace{\int_{a_i}^{c_i} f_\alpha^{\text{G.S.}}n_\beta\Phi\,\mathrm{d}\theta}_{\text{gross slip}} + \underbrace{\int_{c_i}^{d_i} f_\alpha^{\text{M.S.}}n_\beta\Phi\,\mathrm{d}\theta}_{\text{microslip}}\right],
\tag{2.8}
$$

$$
\mu_\alpha = \frac{1-\upsilon}{\pi R}\sum_{i=1}^{x}\left[\underbrace{\int_{a_i}^{c_i}\left[M^{\text{G.S.}}n_\alpha + Re_{\beta\phi3}f_\beta^{\text{G.S.}}n_\alpha n_\phi\right]\Phi\,\mathrm{d}\theta}_{\text{gross slip}} + \underbrace{\int_{c_i}^{d_i}\left[M^{\text{M.S.}}n_\alpha + Re_{\beta\phi3}f_\beta^{\text{M.S.}}n_\alpha n_\phi\right]\Phi\,\mathrm{d}\theta}_{\text{microslip}}\right],
\tag{2.9}
$$

where the superscripts 'G.S.' and 'M.S.' denote the gross slip and microslip terms, respectively. The integrals corresponding to regions of no contact are not shown, as regions of no contact

do not contribute (directly) to the stress or couple stress. The integration limits and the upper limit of the summation index x obey the following relationships:

$$\sum_{i=1}^{x}[(c_i - a_i) + (d_i - c_i) + (e_i - d_i)] = 2\pi, \quad \text{and} \quad a_1 = 0; \, a_{i+1} = e_i; \, e_x = 2\pi. \tag{2.10}$$

Equation (2.10) is a condition that ensures that all possible contact directions $(0 \rightarrow 2\pi)$ have been assigned a contact mode. In (2.10), the quantity $(e_i - d_i)$ corresponds to the range of angles for which there are no contacts. The gross slip regions $(c_i - a_i)$ are further separated into two regions, $(b_i - a_i)$ and $(c_i - b_i)$, which are related to sign (Δu^t) being positive or negative, respectively. The limits of integration in (2.8) and (2.9) need to be determined from the inequality constraints in (2.5) and (2.7). For example, the limits a_i, c_i and d_i, demarcating the regions of gross slip and microslip, must satisfy $k^t |\Delta u^t| - \mu |f^n| = 0$. The integration limits a_i, d_i and e_i satisfy $f^n = 0$, and the gross-slip integration limit b_i must satisfy $(\varepsilon_{qr} n_r t_q - R n_\varphi \kappa_\varphi) = 0$. If, for example, with increasing angle a gross slip region $(c_3 - b_3)$ is immediately followed by a region of no contact $(e_3 - d_3)$, the microslip integration limits are set to have the property $d_3 = c_3 = 0$. These integration limits will now be referred to as the transition angles. Due to the form of the constraints in (2.5) and (2.7), involving absolute values of cosine-squared functions, there exists an upper bound on the value that the summation index x may take.

A linear contact law is used to approximate the rolling resistance for both the microslip and gross slip contacts, such that

$$M^{\text{G.S.}} = 2k'^{\text{G.S.}} R k_\psi n_\psi, \tag{2.11}$$

$$M^{\text{M.S.}} = 2k'^{\text{M.S.}} R k_\psi n_\psi, \tag{2.12}$$

where $k'^{\text{G.S.}}$ and $k'^{\text{M.S.}}$ are rolling-stiffness coefficients.

In this paper, the bipolar form for the contact-density distribution function Φ used by Walsh and Tordesillas [4] is adopted (see Equation (1.3) and Figure 2). However, unlike in [4], no assumption is imposed on the direction of maximum probability of finding a contact $\boldsymbol{m}$ (direction of contact anisotropy) at this stage of the analysis. Hence, the direction of $\boldsymbol{m}$ can be defined at the point of implementation of the resulting constitutive law. Furthermore, in the present analysis, the form of Φ and the direction of $\boldsymbol{m}$ serve only as *initial* conditions for the contact anisotropy. Since the contact laws introduced earlier incorporate loss of contacts, then, as deformation proceeds, the contact-density distribution function will be, in effect, modified (evolving) as various angles are "switched off" for regions in which particle contacts are broken.

We note that the bipolar form of Φ is based on a numerical simulation of the direction of contacts averaged over a large number of particles [3]. Furthermore, the generalised constitutive equations (1.1) and (1.2) are not restricted to a specific particle-cluster configuration, which was the original reason for Tordesillas and Walsh [1] to introduce the weighting function Φ. Therefore, when interpreting the contact mode and force anisotropy results in Section 4 of this paper, we emphasize that the results will be an *expectation* rather than an exact prediction of the contact behaviour within a granular specimen.

The form of Φ in Equation (1.3) is now substituted in Equations (2.8) and (2.9), along with the expressions for the contact forces and moments (2.3), (2.5), (2.11) and (2.12). With these substitutions, Equations (2.8) and (2.9) can be integrated to give the following micro-mechanical constitutive laws:

$$\sigma_{\alpha\beta} = a(\upsilon)\left[P_{\alpha\beta} + Q_{\alpha\beta mn}\varepsilon_{mn} + R_{\alpha\beta j}\varepsilon_{\alpha j} + S_{\alpha\beta sj}\varepsilon_{sj}\right], \tag{2.13}$$

$$\mu_\alpha = a(\upsilon) T_{\alpha\psi}\kappa_\psi, \tag{2.14}$$

where

$$a(\upsilon) = \frac{1}{2\pi R}\left[\frac{(1-\upsilon)\left[36 - 4\pi\sqrt{3}\right] - \pi^2}{6 - \pi\sqrt{3}}\right]. \tag{2.15}$$

The coefficients $P_{\alpha\beta}$, $Q_{\alpha\beta mn}$, $R_{\alpha\beta j}$, $S_{\alpha\beta sj}$ and $T_{\alpha\psi}$ depend on the transition angles, the various anisotropy parameters and the physical properties of particles, and are defined in the Appendix. To obtain (2.15) it has been assumed, following Hinrichsen *et al.* [7], that

$$N = \frac{1}{6 - \pi\sqrt{3}}\left[36 - 4\pi\sqrt{3} - \frac{\pi^2}{1-\upsilon}\right], \tag{2.16}$$

for $0 \le N \le 6$. Equation (2.16) reflects an expected relationship between the number of contacts per particle and the void ratio and, in a similar manner to (1.3), it was obtained by averaging over a large number of particles. As such, any results obtained using (2.16) will be considered to reflect an average or expectation rather than an exact prediction for a specific particle cluster.

3. Fabric and force evolution in a bi-axial compression test

To demonstrate the capabilities of the micromechanically-based constitutive model, we examine the formation of shear bands in a bi-axial test, using the method provided by Mühlhaus and Vardoulakis [8] for micropolar continua. As illustrated in Figure 4, the specimen is compressed in the X_2-direction at a constant rate. The vertical boundaries are allowed to deform such that the normal stress σ_{11} remains constant along these boundaries. Prior to shear-band formation, the deformation is assumed to be homogeneous and $\varepsilon_{12} = \varepsilon_{21} = \kappa_1 = \kappa_2 = 0$. In addition to predicting shear-band evolution, specific attention will be given to the model's predictions of microstructural development (*e.g.* contact and contact-force evolution).

Briefly, the method originally proposed by Mühlhaus and Vardoulakis [8] involves solving the rate form of the stress equilibrium equations for a Cosserat/micropolar material, and then looking for special solutions that may exist within a narrow region (shear band). These special solutions correspond to an inhomogeneous deformation that is distinct from the homogeneous deformation occurring both prior to the onset of a shear band and outside the shear band after the band has formed. The onset of the inhomogeneous solution is referred to as the bifurcation point.
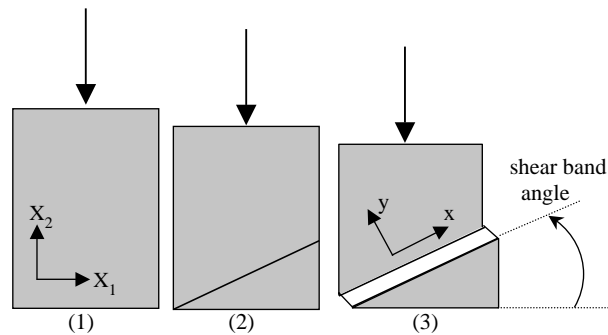

Figure 4. Stages in shear-band formation within a bi-axial test: (a) initial specimen, (1) homogeneous deformation prior to shear band formation, (2) onset of shear band or bifurcation point, and (3) evolution of shear band.

Adopting the nomenclature employed by Tordesillas *et al.* [9], we can write the stress-rate equilibrium equations in shear-band coordinates (x, y) in terms of time rates of displacement V and rotation $\dfrac{d\omega}{dt}$ as:

$$A_{\alpha\eta} V_\eta'' + A_{\alpha 31} \frac{d\omega''}{dt} + A_{\alpha 32} \frac{d\omega'}{dt} = 0, \tag{3.1}$$

$$A_{3\eta 1} V_\eta'' + A_{3\eta 2} V_\eta' + A_{331} \frac{d\omega''}{dt} + A_{332} \frac{d\omega'}{dt} + A_{333} \frac{d\omega}{dt} = 0, \tag{3.2}$$

where only the gradients across the shear band (the y-coordinate) are nonzero with $(\ )' = \dfrac{d(\ )}{dy}$; $\alpha = 1, 2$; $\eta = 1, 2$; and the various coefficients (*i.e.*, the subscripted 'A's) come from the rate form of the constitutive law. That is, by writing

$$\left\langle \frac{d\sigma_{\alpha\beta}}{dt} \right\rangle = L_{\alpha\beta\eta\lambda} \frac{d\varepsilon_{\eta\lambda}}{dt}, \tag{3.3}$$

$$\left\langle \frac{d\mu_\lambda}{dt} \right\rangle = G_{\lambda\alpha\beta} \frac{d\varepsilon_{\alpha\beta}}{dt} + H_{\lambda\alpha} \frac{d\kappa_\alpha}{dt}, \tag{3.4}$$

where $\langle \ \rangle$ represent the Jaumann time derivative, we can be represent the various coefficients in (3.1) and (3.2) as

$$A_{11} = s_\lambda s_1 L_{111\lambda} + s_\lambda s_2 L_{121\lambda} - \frac{1}{2} s_2 s_2 \sigma, \quad A_{12} = s_\lambda s_1 L_{112\lambda} + s_\lambda s_2 L_{122\lambda} + \frac{1}{2} s_1 s_2 \sigma,$$

$$A_{21} = s_\lambda s_1 L_{211\lambda} + s_\lambda s_2 L_{221\lambda} - \frac{1}{2} s_1 s_2 \sigma, \quad A_{22} = s_\lambda s_1 L_{212\lambda} + s_\lambda s_2 L_{222\lambda} + \frac{1}{2} s_1 s_1 \sigma,$$

$$A_{132} = e_{\eta\lambda 3} s_1 L_{11\eta\lambda} + e_{\eta\lambda 3} s_2 L_{12\eta\lambda}, \quad A_{232} = e_{\eta\lambda 3} s_2 L_{22\eta\lambda} + e_{\eta\lambda 3} s_1 L_{21\eta\lambda},$$

$$A_{131} = A_{231} = 0, \quad A_{311} = s_\lambda s_1 G_{11\lambda} + s_\lambda s_2 G_{21\lambda},$$

$$A_{321} = s_\lambda s_1 G_{12\lambda} + s_\lambda s_2 G_{22\lambda}, \quad A_{312} = s_\lambda L_{211\lambda} - s_\lambda L_{121\lambda},$$

$$A_{322} = s_\lambda L_{212\lambda} - s_\lambda L_{122\lambda}, \quad A_{331} = H_{1\lambda} s_\lambda s_1 + H_{2\lambda} s_\lambda s_2,$$

$$A_{332} = e_{\eta\lambda 3} s_1 G_{1\eta\lambda} + e_{\eta\lambda 3} s_2 G_{2\eta\lambda}, \quad A_{333} = e_{\eta\lambda 3} L_{21\eta\lambda} - e_{\eta\lambda 3} L_{12\eta\lambda}. \tag{3.5}$$

In Equation (3.5), $\sigma = \sigma_{11} - \sigma_{22}$, $s_1 = -\sin\theta_b$ and $s_2 = \cos\theta_b$, where θ_b is the shear-band angle (see Figure 4).

Solutions are then sought for (3.1) which satisfy the following boundary conditions (in accordance with experimental observations and DEM simulations of Iwashita and Oda [5] and Oda and Kazama [10]:

(i)   across a shear band (*i.e.*, $-d_b \geq y \geq d_b$ where $2d_b$ is the shear-band thickness), the displacement rate is an even function of y and the rotation rate is an odd function of y;

(ii)   continuity of traction and couple stress at the shear-band boundary;

(iii) $V_1 = \frac{V_1^*}{2}$ and $V_2 = \frac{V_2^*}{2}$ at $y = d_b$ and $V_1 = -\frac{V_1^*}{2}$ and $V_2 = -\frac{V_2^*}{2}$ at $y = -d_b$. Since it is assumed that regions outside the shear band act rigidly after the bifurcation strain is reached, and that the bi-axial test is strain-controlled, the rate of vertical displacement of the rigid outer regions of the specimen V_2^* is prescribed. The horizontal rate of displacement V_1^*, on the other hand, needs to be determined from the strain within the shear band.

Once the displacement and rotation rates are determined, from solving (3.1) and (3.2) subject to the boundary conditions, an incremental procedure can be adopted to determine the strain and rotation within a shear band, and therefore the evolution of the shear band. For a more detailed discussion of the shear-banding problem and the method outlined here, see [9].

4. Results and discussion

Prior to deformation, we assume that the particles are randomly packed under conditions in which gravity is negligible. Therefore, the expected contact distribution and the expected contact-force distribution are isotropic, *i.e.*, $\chi = \chi^* = 0$. Only after deformation occurs would one expect the contact distribution and the contact-force distribution to become anisotropic and take on a preferential direction. Model predictions are now presented for the following model parameters: $\chi = \chi^* = 0$; $m_2 = 1$; $v_0 = 0.2$; $\phi = 0$; $f^{\text{initial}} = -(1/20)Rk^n$; $k^n = k^t = 4 \times 10^7$ N/m; $R = 0.005$ m. These parameters reflect a moderate particle-packing density with an initially isotropic contact and contact-force distribution.

Figure 5 shows the change in thickness of a shear band inclined at an angle of 65 degrees to the X_1-axis. The thickness rapidly approaches a value of 4–5 particle diameters. In real sands for which there is a distribution of particle sizes and shapes, reported shear-band widths range from around 7–8 particle diameters [10] up to 17 particle diameters [11]. However, two-dimensional Schneebeli systems, consisting of circular rods, display shear bands that involve fewer particles (1–4 particle diameters) than those found in real sands [12]. Note that the thickness predicted by the current model is also consistent with the shear-band analysis based on the deformation theory of plasticity for frictional materials with internal constraint [8], [13]. Although not shown, other shear-band inclinations display similar behaviour.

In Figure 6, it can be seen that the expected contact distribution evolves with increasing strain. Stage 1, the innermost (smallest) ring, corresponds to the initial contact mode distribution. Stage 2, the middle ring, corresponds to the contact-mode distribution at the bifurcation point (onset of shear banding). Stage 3, the outside (largest) ring, corresponds to the contact mode distribution within a shear band at a shear strain of 0.8. Initially, all contacts are microslip contacts (stage 1). With compression, however, contacts are lost in the direction perpendicular to the applied compressive strain, and the regions of microslip shrink to a narrow angle in the direction of the maximum principal strain (stage 2). This pattern of loss and retention of contacts is consistent with the formation of particle columns at the onset
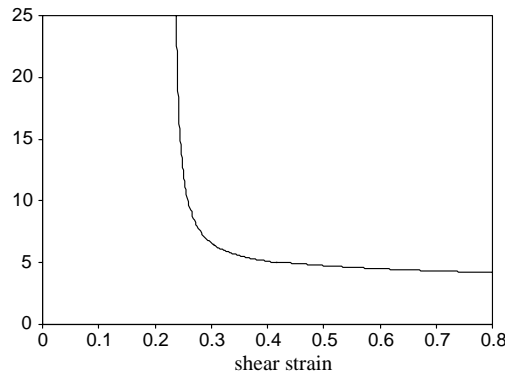

Figure 5. The variation of the shear-band thickness with shear strain for a shear band inclined at 65 degrees to the X_1-axis.
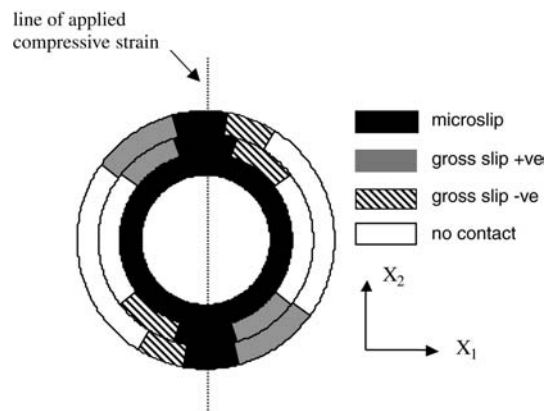
Figure 6. Evolution of contact modes for the three stages of the bi-axial test.
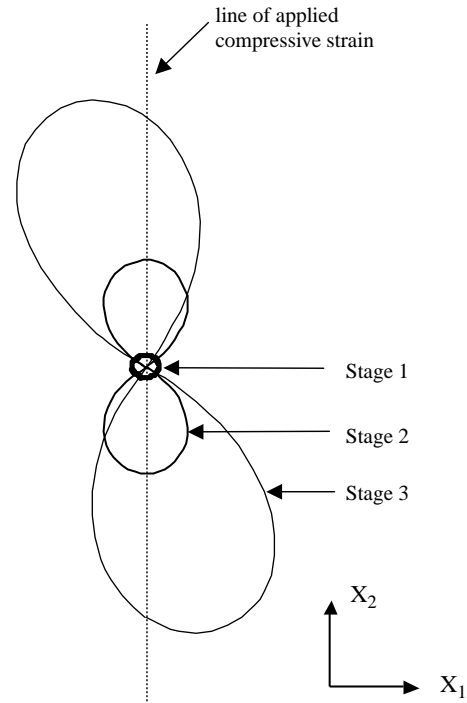
Figure 7. A polar plot showing the evolution of the normal contact force for the three stages of the bi-axial test.

of shear banding. It is thought that the buckling of these particle columns is the underlying mechanism responsible for the softening observed during shear banding [10]. With a further increase in shear strain it is seen that there is a rotation of the direction of contacts (and no contacts) and the contact modes, which is also consistent with observed microstructural development inside shear bands (stage 3).

Figure 7 displays the evolution of the normal contact force for the three stages in shear-band development presented in Figure 6. Firstly, it is confirmed that normal contact-force anisotropy can develop from an initially isotropic distribution using this constitutive model. At the bifurcation point the normal contact force has become highly anisotropic, with a maximum direction aligned with the maximum principal strain. Secondly, within the shear band, the direction of the maximum normal force begins to rotate away from the direction of maximum principal strain. The direction and rate of rotation of the normal contact force is the same as the direction of rotation of the contact modes shown in Figure 6, and the combined contact mode and normal contact force behaviour is consistent with the rotation of particle columns and force chains in a shear band.

Figure 8 shows the change in the *global* void ratio (void ratio averaged across the entire specimen) for stage 1, and the change in the *local* void ratio (void ratio averaged across the band) during stage 3. The initial overall compaction by an applied compressive strain is expected, given that the initial void ratio is 0·2. The observed decrease in void ratio of 0·05 corresponds to an average gain of only one contact per particle. At first glance this result would seem to contradict the loss of contacts observed in Figure 6. However, one should recall that: (i) the contact modes are only expectations, and (ii) a void ratio of 0·2 only cor-
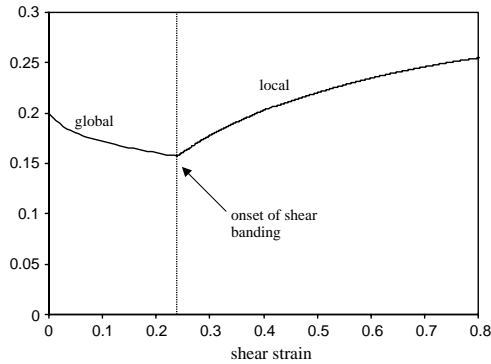
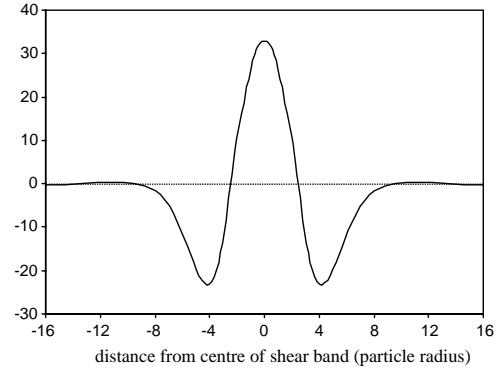*Figure 8.* The variation of void ratio with deformation.

Figure 9. Total rotation in the region of the shear band at a shear strain of 0·8.

responds to approximately three contacts per particle, such that a particle can readily accommodate an additional contact within the region predicted to have a contact in Figure 6. The increase in void ratio within a shear band, as shown in Figure 8, is consistent with the experimental observations of dilation and the appearance of large voids within shear bands in sands (*e.g.* see [2, Chapter 4]) and assemblies Schneebeli rods [12].

The total rotation in the region of the shear band, as shown in Figure 9, refers to the net accumulation of rotation ω (see Equation (3.1)) from the start of deformation up to a shear strain of 0·8. Note that although the shear band thickness at a shear strain of 0·8 is only 4–5 particle diameters (Figure 5), the microstructure beyond 5 particle diameters has been disturbed (finite rotations) due to prior shear strains for which the shear band thickness was greater than 5 particle diameters. The shear-band thickness shown in Figure 5 should then be considered an instantaneous thickness, whereas a shear-band thickness implied by rotations should resemble that seen in experiments.

Note that the current model predicts rotations to change sign within a shear band. This would seem to contradict the findings from DEM simulations of Iwashita and Oda [5], in which particles were seen to rotate in one direction on average. It could be argued that, as the shear-band thickness in Figure 5 is in the range of 4–5 particle diameters, beyond a shear strain of 0·8, further rotations will only occur within 4–5 particle radii from the centre of the shear band, such that the central, unidirectional, peak will begin to dominate the observed rotations. However, larger shear strains are beyond the small strain limitations of the current constitutive model.

5. Conclusions

A high-resolution, micromechanically-based, Cosserat constitutive model for the quasi-static deformation of a dry granular material has been presented. The model incorporates inter-particle contacts undergoing microslip, gross slip, rolling resistance and loss of contact. Fabric and contact force anisotropies are also introduced, and the evolution of these anisotropies is naturally accounted for. When applied to the shear-banding problem, the micromechanically-based constitutive laws successfully reproduces expected shear-band thicknesses and the contact and force anisotropies evolve in a way consistent with the formation and evolution of particle columns and force chains within a shear band. Ongoing work is focused on understanding the evolution of the anisotropies, through a DEM analysis, in preparation for the extension of these models to the large deformations encountered in engineering applications.

Appendix A. Coefficients appearing in Equation (2.13) and (2.14)

The various coefficients in the constitutive equations (2.13) and (2.14) are

$$P_{\alpha\beta} = \frac{f^{\text{initial}}}{\pi} \sum_{i=1}^{x} \left[\begin{array}{l} w_1\left(a_i, d_i\right) W_{\alpha\beta1} + w_2\left(a_i, d_i\right) W_{\alpha\beta2} + w_3\left(a_i, d_i\right) W_{\alpha\beta3} \\ +\mu e_{s\alpha3} \left[\begin{array}{l} \left(w_1\left(b_i, c_i\right) - w_1\left(a_i, b_i\right)\right) W_{s\beta1} + \left(w_2\left(b_i, c_i\right) - w_2\left(a_i, b_i\right)\right) W_{s\beta2} \\ + \left(w_3\left(b_i, c_i\right) - w_3\left(a_i, b_i\right)\right) W_{s\beta3} \end{array} \right] \end{array} \right],$$

$$Q_{\alpha\beta mn} = \frac{2Rk^n}{\pi} \sum_{i=1}^{x} \left| \begin{array}{l} w_4\left(a_i, d_i\right) W_{\alpha\beta1} W_{mn1} + w_5\left(a_i, d_i\right) \left(W_{\alpha\beta1} W_{mn2} + W_{\alpha\beta2} W_{mn1}\right) \\ + w_6\left(a_i, d_i\right) \left(W_{\alpha\beta1} W_{mn3} + W_{\alpha\beta2} W_{mn2} + W_{\alpha\beta3} W_{mn1}\right) \\ + w_7\left(a_i, d_i\right) \left(W_{\alpha\beta2} W_{mn3} + W_{\alpha\beta3} W_{mn2}\right) + w_8\left(a_i, d_i\right) W_{\alpha\beta3} W_{mn3} \\ +\mu e_{s\alpha3} \left| \begin{array}{l} \left(w_4\left(b_i, c_i\right) - w_4\left(a_i, b_i\right)\right) W_{s\beta1} W_{mn1} \\ + \left(w_5\left(b_i, c_i\right) - w_5\left(a_i, b_i\right)\right) \left(W_{s\beta1} W_{mn2} + W_{s\beta2} W_{mn1}\right) \\ + \left(w_6\left(b_i, c_i\right) - w_6\left(a_i, b_i\right)\right) \left(W_{s\beta1} W_{mn3} + W_{s\beta2} W_{mn2} + W_{s\beta3} W_{mn1}\right) \\ + \left(w_7\left(b_i, c_i\right) - w_7\left(a_i, b_i\right)\right) \left(W_{s\beta2} W_{mn3} + W_{s\beta3} W_{mn2}\right) \\ + \left(w_8\left(b_i, c_i\right) - w_8\left(a_i, b_i\right)\right) W_{s\beta3} W_{mn3} \end{array} \right| \end{array} \right|,$$

$$R_{\alpha\beta j} = \frac{2Rk^t}{\pi} \sum_{i=1}^{x} \left[w_9\left(c_i, d_i\right) W_{j\beta1} + w_{10}\left(c_i, d_i\right) W_{j\beta2} + w_{11}\left(c_i, d_i\right) W_{j\beta3} \right]$$

$$S_{\alpha\beta sj} = -\frac{2Rk^t}{\pi} \sum_{i=1}^{x} \left| \begin{array}{l} w_{12}\left(c_i, d_i\right) W_{\alpha\beta1} W_{sj1} + w_{13}\left(c_i, d_i\right) \left(\begin{array}{l} e_{h\alpha3} W_{h\beta1} W_{sj1} + e_{hs3} W_{\alpha\beta1} W_{hj1} \\ + e_{h\beta3} W_{\alpha h1} W_{sj1} + e_{hj3} W_{\alpha\beta1} W_{sh1} \end{array} \right) \\ + w_{14}\left(c_i, d_i\right) \left(\begin{array}{l} W_{j\beta1}\delta_{s\alpha} + W_{js1}\delta_{\beta\alpha} + W_{s\beta1}\delta_{j\alpha} + W_{\alpha\beta1}\delta_{js} \\ + W_{\alpha j1}\delta_{\beta s} + W_{\alpha s1}\delta_{\beta j} - 6 W_{\alpha\beta1} W_{sj1} \end{array} \right) \\ + w_{15}\left(c_i, d_i\right) \left(\begin{array}{l} e_{h\beta3} W_{jh1} W_{s\alpha3} + e_{hj3} W_{h\beta1} W_{s\alpha3} \\ + e_{h\alpha3} W_{sh1} W_{j\beta3} + e_{hs3} W_{h\alpha1} W_{j\beta3} \end{array} \right) \\ + w_{16}\left(c_i, d_i\right) \left(W_{\alpha\beta1} W_{sj1} + \delta_{j\beta}\delta_{s\alpha} - W_{j\beta1}\delta_{s\alpha} - \delta_{j\beta} W_{\alpha s1} \right) \end{array} \right|,$$

$$T_{\alpha\psi} = \frac{2R}{\pi} \sum_{i=1}^{x} \left[\begin{array}{l} k^{G.S.} \left[w_9\left(a_i, c_i\right) W_{\alpha\psi1} + w_{10}\left(a_i, c_i\right) W_{\alpha\psi2} + w_{11}\left(a_i, c_i\right) W_{\alpha\psi3} \right] \\ + \left(k^{M.S.} + R^2 k^t\right) \left[w_9\left(c_i, d_i\right) W_{\alpha\psi1} + w_{10}\left(c_i, d_i\right) W_{\alpha\psi2} + w_{11}\left(c_i, d_i\right) W_{\alpha\psi3} \right] \end{array} \right],$$

where

$$\delta_{\alpha\beta} = \begin{cases} 1 & \text{if } \alpha = \beta, \\ 0 & \text{if } \alpha \neq \beta, \end{cases}$$

$$W_{\alpha\beta1} = m_\alpha m_\beta,$$

$$W_{\alpha\beta2} = \left[e_{\phi\beta3} W_{\alpha\phi1} + e_{\phi\alpha3} W_{\phi\beta1} \right],$$

$$W_{\alpha\beta3} = \left[\delta_{\alpha\beta} - W_{\alpha\beta1} \right],$$

$$w_1\left(x, y\right) = \frac{1}{48} \left(\begin{array}{l} 12\left(2 + \chi + \left(1 + \chi\right) \chi^* \cos\phi\right)\left(y - x\right) + 3\left(\chi + 4\right) \chi^* \sin\phi\left(\cos 2y - \cos 2x\right) \\ + 3\left(\chi + 1\right) \chi^* \sin\phi\left(\cos 4y - \cos 4x\right) + \chi\chi^* \sin\phi\left(\cos 6y - \cos 6x\right) \\ + 3\left(4\left(\chi + 1\right) + \left(3\chi + 4\right) \chi^* \cos\phi\right)\left(\sin 2y - \sin 2x\right) \\ + 3\left(\chi + \left(\chi + 1\right) \chi^* \cos\phi\right)\left(\sin 4y - \sin 4x\right) + \chi\chi^* \cos\phi\left(\sin 6y - \sin 6x\right) \end{array} \right),$$

$$w_2\left(x, y\right) = \frac{1}{48} \left(\begin{array}{l} 12\chi^* \sin\phi\left(x - y\right) + 3\chi\chi^* \left(\cos\left(\phi - 2x\right) - \cos\left(\phi - 2y\right)\right) \\ + 12\left(\cos 2x - \cos 2y\right) + 3\chi\left(\cos 4x - \cos 4y\right) \\ + 3\chi^* \left(\cos\left(\phi + 4x\right) - \cos\left(\phi + 4y\right)\right) + \chi\chi^* \left(\cos\left(\phi + 6x\right) - \cos\left(\phi + 6y\right)\right) \end{array} \right),$$

$$w_3(x, y) = \frac{1}{48} \begin{vmatrix} 12\,(2 - \chi + (\chi - 1)\,\chi^*\cos\phi)\,(y - x) \\ + 12\,(\chi - 1)\,(\sin 2y - \sin 2x) + 3\chi\,\chi^*\,(\sin(\phi - 2y)) - \sin(\pi - 2x)) \\ + 6\chi^*\,(2 - \chi)\,(\sin(\phi + 2y) - \sin(\phi + 2x)) - 3\chi\,(\sin 4y - \sin 4x) \\ + 3\chi^*\,(\chi - 1)\,(\sin(\phi + 4y) - \sin(\phi + 4x)) - \chi\,\chi^*\,(\sin(\phi + 6y) - \sin(\phi + 6x)) \end{vmatrix},$$

$$w_4(x, y) = \frac{1}{96}\begin{pmatrix} 3\,(8\chi + 12)\,(y - x) + 3\,(7\chi + 8)\,(\sin 2y - \sin 2x) \\ + 3\,(2\chi + 1)\,(\sin 4y - \sin 4x) + \chi\,(\sin 6y - \sin 6x) \end{pmatrix},$$

$$w_5(x, y) = \frac{1}{96}\,(3\,(\chi + 4)\,(\cos 2x - \cos 2y) + 3\,(\chi + 1)\,(\cos 4x - \cos 4y) + \chi\,(\cos 6x - \cos 6y)),$$

$$w_6(x, y) = \frac{1}{96}\,(12\,(y - x) + 3\chi\,(\sin 2y - \sin 2x) - 3\,(\sin 4y - \sin 4x) - \chi\,(\sin 6y - \sin 6x)),$$

$$w_7(x, y) = \frac{1}{96}\,(3\,(\chi - 4)\,(\cos 2y - \cos 2x) - 3\,(\chi - 1)\,(\cos 4y - \cos 4x) + \chi\,(\cos 6y - \cos 6x)),$$

$$w_8(x, y) = \frac{1}{96}\begin{pmatrix} 3\,(-8\chi + 12)\,(y - x) - 3\,(-7\chi + 8)\,(\sin 2y - \sin 2x) \\ + 3\,(-2\chi + 1)\,(\sin 4y - \sin 4x) + \chi\,(\sin 6y - \sin 6x) \end{pmatrix},$$

$$w_9(x, y) = \frac{1}{16}\,(4\,(2 + \chi)\,(y - x) + 4\,(1 + \chi)\,(\sin 2y - \sin 2x) + \chi\,(\sin 4y - \sin 4x)),$$

$$w_{10}(x, y) = \frac{1}{8}\,(\cos 2x - \cos 2y)\,(2 + \chi\,(\cos 2x + \cos 2y)),$$

$$w_{11}(x, y) = \frac{1}{16}\,(4\,(2 - \chi)\,(y - x) + 4\,(\chi - 1)\,(\sin 2y - \sin 2x) - \chi\,(\sin 4y - \sin 4x)),$$

$$w_{12}(x, y) = \frac{1}{96}\begin{pmatrix} (36 + 24\chi)\,(y - x) + 3\,(8 + 7\chi)\,(\sin 2y - \sin 2x) \\ + 3\,(1 + 2\chi)\,(\sin 4y - \sin 4x) + \chi\,(\sin 6y - \sin 6x) \end{pmatrix},$$

$$w_{13}(x, y) = \frac{1}{48}\,(\cos 2x - \cos 2y)\begin{pmatrix} 6 + 2\chi + 3\,(1 + \chi)\,(\cos 2x + \cos 2y) + \chi\,(\cos 4x + \cos 4y) \\ + \chi\cos[2\,(x - y)] + \chi\cos[2\,(x + y)] \end{pmatrix},$$

$$w_{14}(x, y) = \frac{1}{96}\,(12\,(y - x) + 3\chi\,(\sin 2y - \sin 2x) - 3\,(\sin 4y - \sin 4x) - \chi\,(\sin 6y - \sin 6x)),$$

$$w_{15}(x, y) = \frac{1}{96}\begin{pmatrix} 6\chi\,(\cos^2 2x - \cos^2 2y) + 3\,(\chi - 4)\,(\cos 2y - \cos 2x) \\ + 3\,(\cos 4y - \cos 4x) + \chi\,(\cos 6y - \cos 6x) \end{pmatrix},$$

$$w_{16}(x, y) = \frac{1}{96}\begin{pmatrix} (36 - 24\chi)\,(y - x) + 3\,(7\chi - 8)\,(\sin 2y - \sin 2x) \\ - 3\,(2\chi - 1)\,(\sin 4y - \sin 4x) + \chi\,(\sin 6y - \sin 6x) \end{pmatrix}.$$

For the incremental procedure outlined in Section 3, the change in the void ratio from an initial void ratio v_0 is given by

$$v - v_0 = \frac{\text{Area} - \text{Area of particles}}{\text{Area}} - \frac{\text{Initial Area} - \text{Area of particles}}{\text{Initial Area}}$$

$$= (1 - v)\left[\frac{\text{Area} - \text{Initial Area}}{\text{Initial Area}}\right],$$

if ε_{11} and ε_{22} are much larger than ε_{12} and ε_{21} yet still much smaller than 1, $v_0 \ll 1$ and $v \ll 1$, then the change in void ratio can be approximated by $v - v_0 = (1 - v_0)\,[\varepsilon_{11} + \varepsilon_{22}]$.

Acknowledgements

References

1. A. Tordesillas and S.D.C. Walsh, Incorporating rolling resistance and contact anisotropy in micromechanical models of granular media, *Powder Technol.* 124 (2002) 106–111.

2. M. Oda and K. Iwashita (eds.), *Mechanics of Granular Materials: an Introduction*. A.A. Rotterdam: Balkema (1999) 383 pp.

3. L. Rothenburg, R.J. Bathurst and M.B. Dusseault, *Micromechanical Ideas in Constitutive Modelling of Granular Materials*, In: J. Biarez and R. Gourves, (eds.), *Powders and Grains*. Rotterdam: Balkema, (1989) 355–363.

4. S.D.C. Walsh and A. Tordesillas, Stranger than friction – micromechanics of granular media. In: S. Shoop and G. Blaisdell (eds.), *Proceedings, 14th International Conference of the ISTVS*. Vicksburg, Mississippi, USA (2002) pp. 1–10.

5. K. Iwashita and M. Oda, Micro-deformation mechanism of shear banding process based on modified distinct element method. *Powder Technol.* 109 (2000) 192–205.

6. D. Howell, R.P. Behringer and C. Veje, Stress fluctuations in a 2D granular Couette experiment: A continuous transition. *Phys. Rev. Lett.* 82 (1999) 5241–5244.

7. H.J. Hinrichsen, J. Feder and T. Jøssang, Random packing of disks in two dimensions. *Phys. Rev. A* 41 (1990) 4199–4209.

8. H.B. Mühlhaus and I. Vardoulakis, The thickness of shear bands in granular materials. *Geotechnique* 37 (1987) 271–283.

9. A. Tordesillas, J.F. Peters and B.S. Gardiner, Shear band evolution and accumulated microstructural development in Cosserat Media. *Int. J. Num. Analyt. Methods Geomech.* 28 (2004) 981–1010.

10. M. Oda and H. Kazama, Microstructure of shear bands and its relation to the mechanisms of dilatancy and failure of dense granular soils. *Geotechnique* 48 (1998) 465–481.

11. W.W. Harris, G. Viggiani, M.A. Mooney and R.J. Finno, Use of stereophotogrammetry to analyze the development of shear bands in sand. *Geotechn. Testing J.* 18 (1995) 405–420.

12. F. Calvetti, G. Combe and J. Lanier, Experimental micro-mechanical analysis of a 2D-granular material: Relation between structure evolution and loading path. *Mech. Cohesive-Frictional Mater.* 2 (1997) 121–163.

13. J.P. Bardet and J. Proubet, Shear-band analysis in idealized granular material. *J. Engng. Mech.* 118 (1992) 397–415.